

---

# Ultrahigh Frequency Shear-Horizontal Acoustic Wave Humidity Sensor with Ternary Nanocomposite Sensing Layer

Yanghui Liu<sup>1</sup>, Jian Zhou<sup>1,\*</sup>, Shenyu Wen<sup>1</sup>, Yiqin Chen<sup>1</sup>, YongQing Fu<sup>2</sup>, Huigao Duan<sup>1</sup>

1 College of Mechanical and Vehicle Engineering, Hunan University, Changsha 410082, China

2 Faculty of Engineering and Environment, Northumbria University, Newcastle upon Tyne NE1 8ST, United Kingdom

\* Corresponding E-mail: [jianzhou@hnu.edu.cn](mailto:jianzhou@hnu.edu.cn)

**Abstract:** Surface acoustic wave (SAW) technology is promising for humidity monitoring due to its digital output, small size, large-scale production and wireless passive capability, but there are major challenges to achieve ultra-high sensitivity and fast responses using the conventional SAW devices. Herein, ultrahigh frequency (4.7 GHz and 5.9 GHz) shear-horizontal (SH) SAW devices were developed and a ternary nanocomposite strategy of graphene quantum dots/polyethyleneimine/silicon dioxide nanoparticles (GQDs-PEI-SiO<sub>2</sub> NPs) was proposed as a sensitive layer to achieve ultrahigh sensitivity and fast response. This ternary material system was constructed by modifying the surface of SiO<sub>2</sub> NPs with the PEI through an electrostatic force, and then adsorbing the GQDs onto the PEI through hydrogen bonds. Compared with the conventional low frequency SAW devices, the ultrahigh frequency SH-SAW devices showed exceptionally ultra-high sensitivity (2.4 MHz/%RH, 1000 times as high as a 202 MHz SAW device), fast response (20s/5s), excellent linearity, and good repeatability in the range of 20-80% RH. These superior performances are attributed to ultrahigh frequency of SAW devices, large specific surface areas of the nanocomposite (which exposed multiple hydrophilic groups in PEI and GQDs), and high vapor pressure of convex spherical curved liquid surface (which accelerated the adsorption and desorption of water molecules).

**KEYWORDS:** Humidity sensor; Ultrahigh frequency; SAW; SH; GQDs-PEI-SiO<sub>2</sub> NPs



---

## 1. Introduction

Humidity is a basic physical quantity which is linked with water or vapor contents in the atmospheric environment and is one of the most basic environmental parameters [1]. Agricultural planting management, microelectronics processing, biomedicine, weather forecasting and many other industries all need to precisely monitor and control humidity [2-4]. According to their sensing principles, the reported humidity sensors can be broadly divided into resistance-type, capacitive-type, optical-type, and resonant-types, the last of which include quartz crystal microbalance and surface acoustic waves (SAWs) [4]. SAWs are generated and characterized by spatially periodic interdigital transducer electrodes on the surface of a piezoelectric substrate. H<sub>2</sub>O or water molecules adsorbed on the surface of SAW sensor will change its resonant frequency or phase angles, mainly due to the changes of the characteristics of sensitive material, including mass loading, conductivity changes, and elastic modulus changes [5]. SAW devices are widely used for humidity detection due to its digital output, low cost, large-scale production and wireless passive capability. For example, Tang et al. [6] reported SAW humidity sensors with porous sol–gel SiO<sub>2</sub> films, and proved that large specific surface areas and porous structures can greatly improve the humidity sensing performance. Le et al. [7] reported SAW humidity sensors with graphene oxide (GO) films as the sensing layer, and reported that the mass loading effect is the main contributor to the sensing mechanism of the graphene-based SAW humidity sensors. Kuznetsova et al. [8] reported that the Sezawa wave mode based SAW humidity sensor with GO films has better performance than the commonly used Rayleigh wave, with a sensitivity of 91 KHz/% RH.

However, current SAW humidity sensors still have many issues, with some of them listed



---

as following.

(1) For SAW humidity sensors based on a mass loading effect, increasing working frequency can greatly enhance the sensitivity of SAW humidity sensor. For example, Kawalec et al. developed a 393 MHz SAW humidity sensor with Nafion coating, with the sensitivity being double higher than that of a 196 MHz SAW device [9]. However, most the currently reported frequencies of SAW humidity sensors are below ~3 GHz. which hinders the achievement of ultrahigh frequency and ultrahigh sensitivity for humidity detection.

(2) For SAW humidity sensors, a sensing layer is typically needed to improve its sensing performance, and it is often required for excellent hydrophilicity, good durability, large specific surface area, and high porosity [10]. Various materials including metal oxides [11], polymers [12], carbon materials [13], transition metal dichalcogenides [14], and MXenes [15] are widely used for humidity sensing. Currently, many humidity sensors using single type of sensing layer material have been reported, but these sensors have quite different limitations, making them unsuitable for various applications. For example, most polymer sensing layer-based humidity sensors showed low sensitivities due to their relatively smaller specific surface areas.[16]. Graphene oxide-based humidity sensor might have swelling effect and relatively low stability in the high relative humidity (RH) range. [17].

Recently, to address the limitations of individual materials, researchers developed different types of nanocomposite sensing materials to improve various sensing properties and broaden their applications. These include Au/TiO<sub>2</sub>/poly(3,4-ethylenedioxythiophene) (PEDOT) [11], 3D architecture graphene/PVA/SiO<sub>2</sub> [12], and GQDs/ZnO NMs [13]. However, there is still a challenge to manufacture SAW humidity sensors with excellent comprehensive sensing



---

performance (e.g., high sensitivity, fast response time, and good repeatability.) but using simple processes.

To solve these critical issues, herein, ultrahigh frequency shear-horizontal (SH) SAW devices with frequencies of 4.7 GHz (SAW wavelength of 600 nm) and 5.9 GHz (SAW wavelength of 400 nm) were developed on LiNbO<sub>3</sub>/SiO<sub>2</sub>/SiC heterogeneous substrate using an electron beam lithography technology, as shown in **Figure 1a**. A ternary composite strategy of graphene quantum dots/polyethyleneimine/silicon dioxide nanoparticles (GQDs-PEI-SiO<sub>2</sub> NPs) was proposed as a sensing layer to achieve both ultrahigh sensitivity and fast responses. The ternary nanocomposites were synthesized in an aqueous solution, and the modified PEI was coated onto the surfaces of SiO<sub>2</sub> NPs by electrostatic forces. The GQDs were adsorbed onto PEI by forming hydrogen bonds with PEI. The SAW humidity sensor was finally obtained by coating nanocomposites of GQDs-PEI-SiO<sub>2</sub> NPs onto the whole surface of ultrahigh frequency SAW devices with an aluminum oxide as an insulation layer. The developed humidity sensors show ultrahigh sensitivity (i.e., 2.4 MHz/%RH, which is 1000 times as high as the conventional 202 MHz SAW device [12], and 80 times as high as the 1.56 GHz SAW device with a sensitive layer of CeO<sub>2</sub> nanoparticles/PVP nanofibers [18]), fast responses (20s/5s), excellent linearity ( $R^2=0.9814$ ), and a good repeatability in the range of 20-80% RH. Finally, the sensing mechanisms of GQDs-PEI-SiO<sub>2</sub> NPs ternary nanocomposites were explored, and the ultrahigh sensitivity and fast response capabilities were attributed to large numbers of exposed hydrophilic species (-OH, -COOH, -NH<sub>2</sub>) and the additional positive pressure of convex spherical curved liquid surface which accelerated the adsorption and desorption of water molecules (**Figure 1a**).



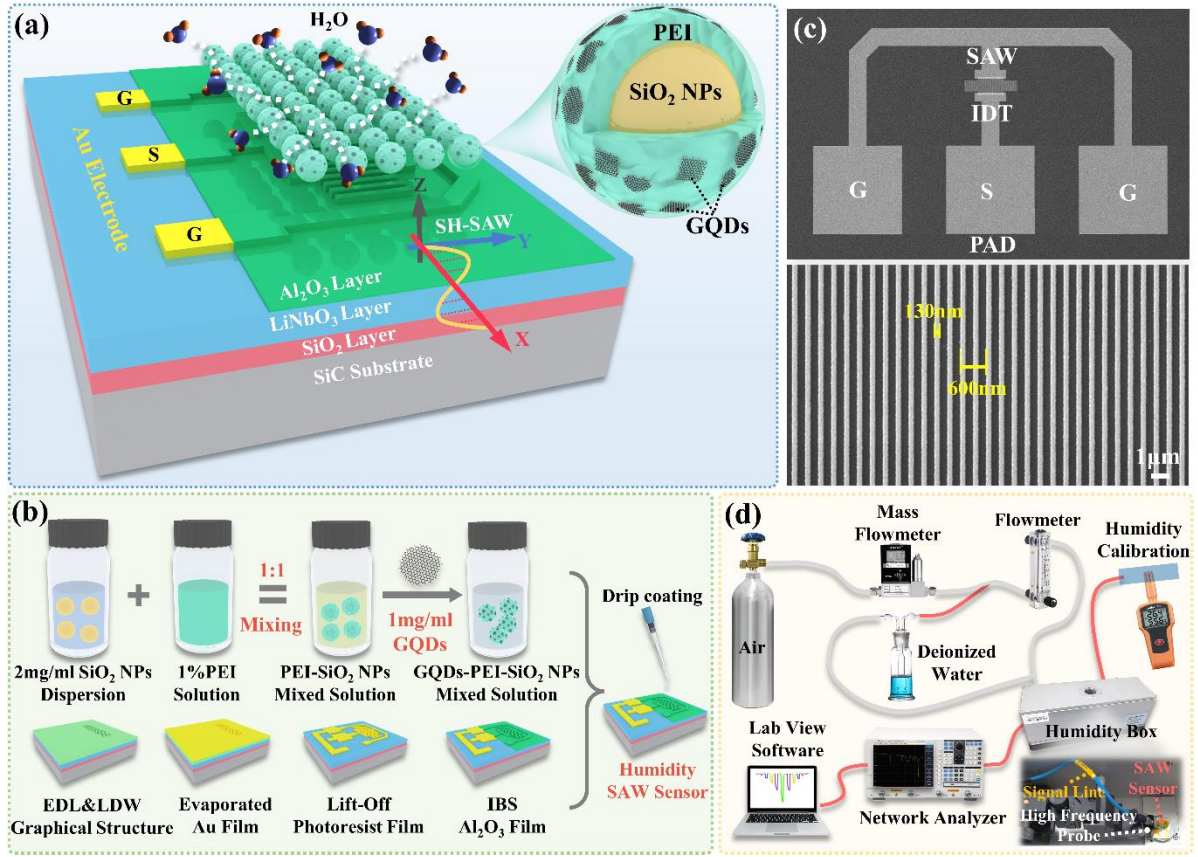


Figure 1: The schematic diagram of ultrahigh frequency SAW humidity sensor with proposed GQDs-PEI-SiO<sub>2</sub> NPs ternary composite material; (b) Preparation process of GQDs-PEI-SiO<sub>2</sub> NPs ternary composite material and ultrahigh frequency SAW humidity sensor; (c) SEM images of ultrahigh frequency SAW device and IDTs ( $\lambda=600\text{nm}$ ); (d) The SAW humidity sensing testing system.

## 2. Experimental section

### 2.1 Preparation and Characterization of GQDs-PEI-SiO<sub>2</sub> NPs

**Figure 1b** shows the detailed preparation processes of the proposed GQDs-PEI-SiO<sub>2</sub> NPs ternary composite material. Firstly, the PEI and SiO<sub>2</sub> NPs were dispersed in deionized water and stirred ultrasonically for 15 minutes to obtain 2 mg/ml SiO<sub>2</sub> NPs solution and 1% PEI solution, respectively. Then, 10 ml SiO<sub>2</sub> NPs solution (2 mg/ml) and 10 ml PEI solution (1%) were mixed in equal volumes, and stirred ultrasonically for 15 minutes to obtain a mixed solution of PEI-SiO<sub>2</sub> NPs. After that, 1 ml GQDs solution (20 mg/ml) was added into 20 ml



---

PEI-SiO<sub>2</sub> NPs mixed solution, and then ultrasonically stirred for 15 minutes to obtain GQDs-PEI-SiO<sub>2</sub> NPs ternary nanocomposites.

Surface morphologies and element distributions of SiO<sub>2</sub> NPs, PEI-SiO<sub>2</sub> NPs and GQDs-PEI-SiO<sub>2</sub> NPs were characterized using a scanning electron microscope (SEM, Sigma-300, Zeiss, Germany) and an energy dispersible spectrometer (EDS, CLARA Xplore 30, TESCAN, Czech Republic). The nanostructures of GQDs, PEI-SiO<sub>2</sub> NPs, and GQDs-PEI-SiO<sub>2</sub> NPs were studied using a transmission electron microscope (TEM, FEI Tecnai 20, America). Chemical bonds in various raw materials and ternary composites were analyzed using a Fourier infrared analyzer (FTIR, Nicolet iS 10, America) and a Raman spectroscopy (Alpha300 access, WITec, Germany). Surface area and porosity were characterized using an Analyzer (JW-BK200C, JWGB SCI.& TECH, China) for SiO<sub>2</sub> NPs, PEI-SiO<sub>2</sub> NPs and GQDs-PEI-SiO<sub>2</sub> NPs.

## 2.2 Preparation of Ultrahigh Frequency SAW Humidity Sensors

The substrate material for fabricating ultrahigh frequency SAW devices was LiNbO<sub>3</sub> (220 nm) film/SiO<sub>2</sub>(130 nm)/SiC, and the crystal cut of LiNbO<sub>3</sub> was 34°Y-X cut. Interdigital transducers (IDTs) of ultrahigh frequency SAWs with wavelengths ( $\lambda$ ) of 600 nm and 400 nm were fabricated using electron beam lithography (EBL) and lift-off processes, by depositing 5 nm Cr/25 nm Au electrodes. Then overlay/alignment process was used to fabricate the bus bar with 5 nm Cr/40 nm Au electrode. After that, the wire bonding pad was obtained using a laser direct writing overlay process with 5 nm Cr/40 nm Au electrode. The overall device manufacturing process is illustrated in **Figure S1**. **Figures 1c** and **S2** present the overall structures and IDT images of the fabricated ultrahigh frequency SAWs with  $\lambda$  of 600 and 400 nm, demonstrating that the fabricated devices have achieved the designed structures, with



---

uniform IDTs' widths without apparent finger breakage or short circuit. 10 nm Al<sub>2</sub>O<sub>3</sub> insulating protective layer was further deposited onto the whole surface of IDTs and bus bars using an ion beam sputtering (IBS) process. For preparing the sensitive layer, a pipette was used to take 0.5 µl volume of GQDs-PEI-SiO<sub>2</sub> NPs solution to drop on surfaces of SAW device. This process was followed by heating the device on a hot plate at 60 °C for 3 minutes to remove excess solvent. The scattering parameters of these ultrahigh frequency SAW devices were measured using a network analyzer (Ceyear, 3656D).

### 2.3 Humidity Tests using Ultrahigh Frequency SAW

**Figure 1d** shows the humidity detection platform with ultrahigh frequency SAW devices. The dry compressed air was served as a carrier gas during the humidity detection and the ambient temperature in the laboratory was maintained at around 25°C. We used a mass flow meter to make sure that total pressure was remained nearly a constant during the experiments. Different RH levels were realized by setting the ratios of dry air (RH=0) and wet air (RH=100%) by adjusting the flow meter. The wet air was generated by flowing dry air through a gas bottle containing water. In the humidity box, high frequency probes and cables were used to transmit signals of the SAW humidity sensor to a network analyzer, and the frequency shifts of SAW humidity sensor under different RH levels were recorded using a LabVIEW program. During the test, a commercial hygrometer was applied to check the RH level inside the humidity chamber.

## 3. Results and Discussion

### 3.1 Characterization of GQDs-PEI-SiO<sub>2</sub> NPs Ternary Nanocomposites

**Figures 2(a~c)** show the surface morphology and element distribution of SiO<sub>2</sub> NPs, PEI-



---

SiO<sub>2</sub> NPs and GQDs-PEI-SiO<sub>2</sub> NPs nanocomposite, and all of them are rough and porous due to the accumulation of numerous nanoparticles. These types of structures provide more adsorption sites for water molecules and improve the sensitivity of humidity sensing. We studied the distributions and contents of Si, O, C and N elements in these types of materials. Element distribution results revealed that, compared with those of single SiO<sub>2</sub> NPs, the PEI-SiO<sub>2</sub> NPs composite shows extra N elements in the material, and the content of C element has been increased, indicating that PEI (which contains C and N elements) has been successfully integrated onto SiO<sub>2</sub> NPs. After the addition of GQDs, the content of C element is significantly increased, as the GQDs contains abundant of C. In addition, the content of N element is also slightly increased, indicating the presence of N element in GQDs, which will be further demonstrated in the subsequent FTIR results. The residual C element in the SiO<sub>2</sub> NPs sample may be due to the inevitable exposure of the sample to air during the testing process.

We further used TEM to investigate microstructures of GQDs, PEI-SiO<sub>2</sub> NPs, and GQDs-PEI-SiO<sub>2</sub> NPs composites. Results shown in **Figure 2d** indicate that the GQDs have particle sizes of 4-12 nm, and the average lattice spacing of GQDs is ~0.28 nm, indicating a similar structure to that of the graphitic carbon [19]. For the PEI-SiO<sub>2</sub> NPs binary nanocomposite as shown in **Figure 2e**, the SiO<sub>2</sub> NPs are covered with a 2-3 nm thick PEI layer, which demonstrates that the PEI is successfully decorated onto the surfaces of SiO<sub>2</sub> NPs for the PEI-SiO<sub>2</sub> NPs composite. In addition, compared with the PEI-SiO<sub>2</sub> NPs composite, there are a large number of GQDs observed on the surfaces of PEI-SiO<sub>2</sub> NPs (**Figure 2f**), illustrating that GQDs are attached to the PEI surface to form GQDs-PEI-SiO<sub>2</sub> NPs ternary composite material.



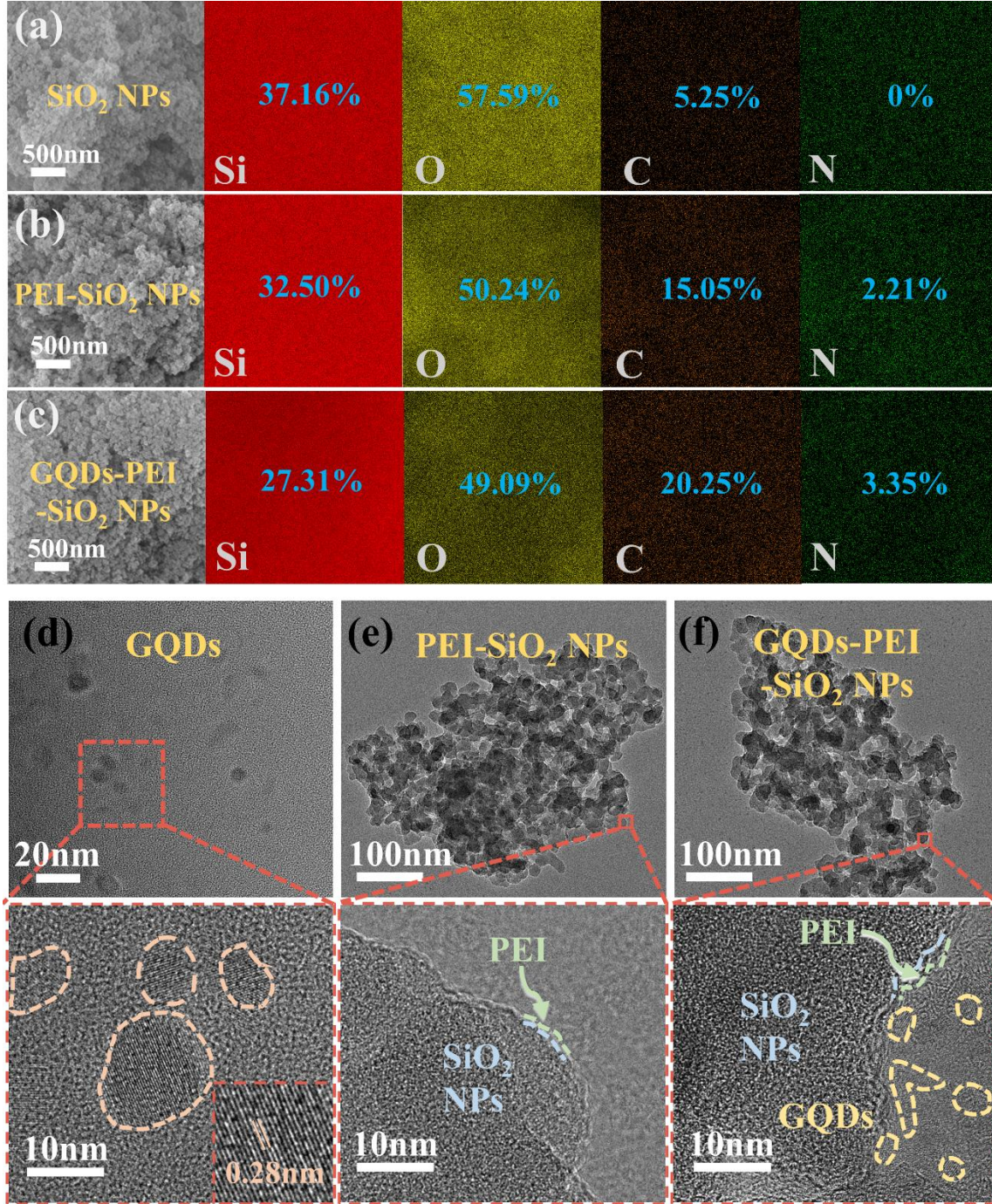


Figure 2: SEM images and EDS elemental images (Si, O, C, and N element) of (a) SiO<sub>2</sub> NPs; (b) PEI-SiO<sub>2</sub> NPs and (c) GQDs-PEI-SiO<sub>2</sub> NPs; TEM images of (d) GQDs; (e) PEI-SiO<sub>2</sub> NPs and (f) GQDs-PEI-SiO<sub>2</sub> NPs.

FTIR and Raman spectroscopy were used to analyze the chemical bonds and functional groups contained in the GQD, PEI, SiO<sub>2</sub> NPs, PEI-SiO<sub>2</sub> NPs and GQDs-PEI-SiO<sub>2</sub> NPs nanocomposites. As shown in **Figure 3a**, there are various peaks in the FTIR spectrum of



---

GQDs including O-H ( $3200\text{ cm}^{-1}$ ), C=O ( $1632\text{ cm}^{-1}$ ), N-H ( $1575\text{ cm}^{-1}$ ), and C-O ( $1395\text{ cm}^{-1}$ ), indicating the presence of -OH, -NH<sub>2</sub>, -COOH on the surface of GQDs [19-21]. This also explains the increase in N element content in the EDS diagram of GQDs-PEI-SiO<sub>2</sub> NPs (**Figure 2c**). For the FTIR results of PEI-SiO<sub>2</sub> NPs, the peaks at 1110, 798, and  $475\text{ cm}^{-1}$  are attributed to the vibrational bands of Si-O-Si stretching vibration, Si-O stretching and Si-O bending vibration in SiO<sub>2</sub> NPs [22], related to the host material of SiO<sub>2</sub> NPs. C-N stretching vibration mode ( $1285\text{ cm}^{-1}$ ), -CH<sub>2</sub> bending vibration mode ( $1456\text{ cm}^{-1}$ ) and N-H bending vibration mode ( $1590\text{ cm}^{-1}$ ) [23] are all observed, indicating the presence of -NH<sub>2</sub> in PEI and also demonstrating that the PEI has been successfully decorated onto SiO<sub>2</sub> NPs [24]. Compared with that of PEI-SiO<sub>2</sub> NPs binary material, the FTIR spectrum of GQDs-PEI-SiO<sub>2</sub> NPs ternary nanocomposite has two weak vibrations modes at 1395 and  $1650\text{ cm}^{-1}$ , caused by the C-O stretching vibration and C=O stretching vibration of GQDs, respectively [20][22]. This proves that GQDs have been successfully modified onto the surfaces of PEI-SiO<sub>2</sub> NPs. FTIR results show that the ternary nanocomposites contain a large number of hydrophilic groups (-OH, -COOH, -NH<sub>2</sub>) which can be used as the hydrophilic sites, for enhancing the sensitivity of humidity sensing.

**Figure 3(b)** shows the characterization results obtained from the Raman spectroscopy. Compared to those of SiO<sub>2</sub> NPs, the additional peaks of 1459, 2874, and  $2956\text{ cm}^{-1}$  in the PEI-SiO<sub>2</sub> NPs are attributed to the -CH and -CH<sub>2</sub> vibration modes of the carbon skeleton in PEI [25]. The spectra of GQDs and GQDs-PEI-SiO<sub>2</sub> NPs show typical graphene characteristics, including the D band ( $1412\text{ cm}^{-1}$ ) caused by defects and symmetrical fractures at the edges of graphene, and a G band ( $1650\text{ cm}^{-1}$ ) caused by in-plane vibration of sp<sup>2</sup> carbon [26]. This once



---

again proves that the GQDs have been successfully integrated into the ternary nanocomposite system. In the graphitic systems, the  $I_D/I_G$  ratio (where  $I_D$  and  $I_G$  are the integrated D and G band intensities, respectively) is an important figure of merit related to the defect density and the crystallite size of carbon materials [26][27]. After adding the GQDs into ternary materials, the  $I_D/I_G$  ratio is increased from 0.9 to 1.32. This indicates an increase in defects in GQDs, which is caused by the hydrogen bonds formed between GQDs and PEI [28].

We further investigate the specific surface areas of the nanocomposites. The results of BET-specific surface areas for  $\text{SiO}_2$  NPs, PEI- $\text{SiO}_2$  NPs, and GQDs-PEI- $\text{SiO}_2$  NPs are 169, 82, and  $96 \text{ m}^2/\text{g}$ , respectively. Results demonstrate that the large specific surface areas in both the composites of PEI- $\text{SiO}_2$  NPs and GQDs-PEI- $\text{SiO}_2$  NPs are mainly induced by the large specific surface area of  $\text{SiO}_2$  NPs. Compared with that of pure  $\text{SiO}_2$  NPs, the decreased specific surface area of PEI- $\text{SiO}_2$  NPs is mainly due to the agglomeration of  $\text{SiO}_2$  NPs caused by the involvement of viscous PEI, which can be verified from the TEM image analysis (**Figure 2e**). For the GQDs-PEI- $\text{SiO}_2$  NPs, a large number of GQDs are attached to the particle surfaces, resulting in an increased surface roughness and an increased specific surface area, if compared with that of the PEI- $\text{SiO}_2$  NPs. Both the PEI- $\text{SiO}_2$  NPs and GQDs- PEI- $\text{SiO}_2$  NPs have large specific surface areas, which are beneficial to expose more hydrophilic species and thus enhance the sensing performance.



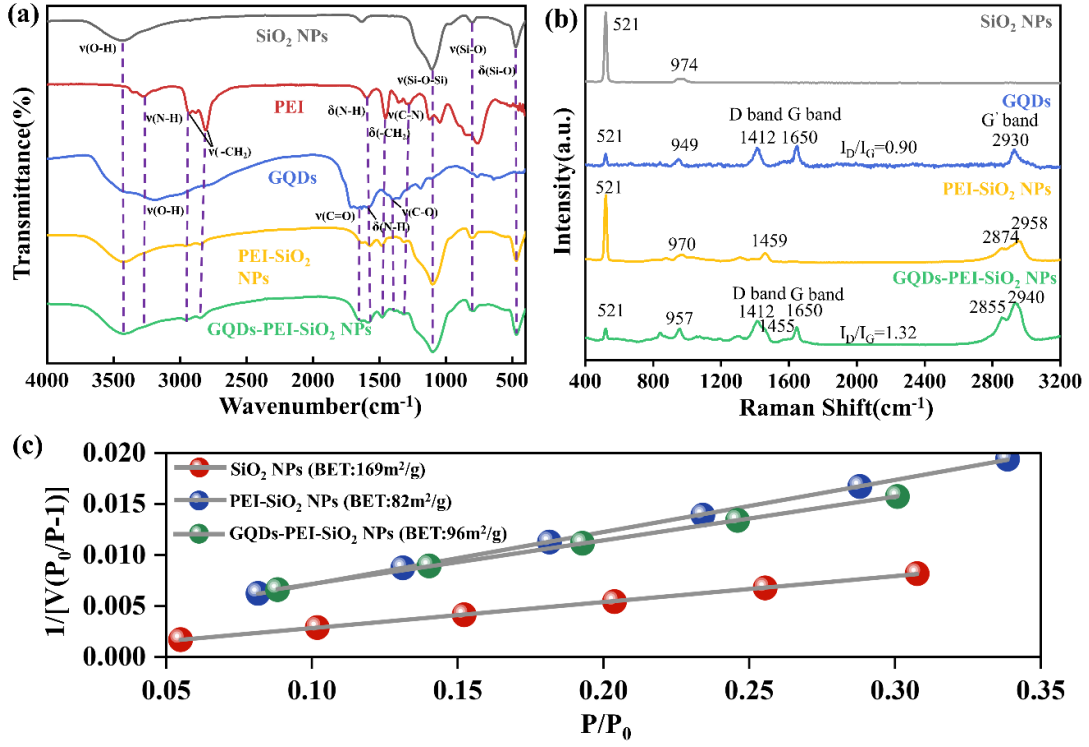


Figure 3: (a) FTIR results of SiO<sub>2</sub> NPs, PEI, GQDs, PEI-SiO<sub>2</sub> NPs, and GQDs-PEI-SiO<sub>2</sub> NPs; (b) Raman spectroscopy results of SiO<sub>2</sub> NPs, GQDs, PEI-SiO<sub>2</sub> NPs, and GQDs-PEI-SiO<sub>2</sub> NPs; (c) BET surface area results of SiO<sub>2</sub> NPs, PEI-SiO<sub>2</sub> NPs and GQDs-PEI-SiO<sub>2</sub> NPs

### 3.2 Humidity Sensing for Ultrahigh Frequency SAW

**Figure 4a** shows the  $S_{11}$  measurement results of the ultrahigh frequency SAW devices (600 nm wavelength), and the corresponding resonant frequency was 4.7 GHz. To analyze this vibration mode, a 3D periodicity model of SAW was established and simulated using the COMSOL software, as shown in **Figure 4b**. The structure parameters of SAW device in simulations are exactly the same with the experimental studies. The thickness of the LiNbO<sub>3</sub> piezoelectric layer was set as 220 nm, the thickness of the SiO<sub>2</sub> layer was 160 nm, the thickness of the Au electrode was 25 nm with its width of  $0.2 \lambda$ , and the thickness of the SiC substrate was set as  $5 \lambda$ . As can be seen from the results shown in **Figure 4b**, the  $Y_{11}$  curve obtained from the simulation is similar with the  $Y_{11}$  curve obtained from the experimental results, which



---

clearly proves the correctness and reliability of the simulation model. **Figure 4a** inset illustrates the particle displacement patterns of this mode (frequency of 4.7GHz) and the vibration of sound waves is mainly concentrated in the Y direction perpendicular to the propagation direction, which clearly demonstrate that the vibration mode is SH-SAW.

**Figures 4c & 4d** show the measured frequency shifts of the ultrahigh frequency SAW humidity sensor ( $\lambda = 600$  nm) at six different humidities conditions (i.e., RH=30%, 40%, 50%, 60%, 70%, 80%) with five cycles. Performance of the SAW humidity sensor (such as frequency shift, response time and recovery time) has not shown apparent changes within 5 cycles of humidity tests, indicating the good repeatability of the fabricated ultrahigh frequency SAW humidity sensors at different humidities conditions.

**Figure 4e** shows the frequency responses of the ultrahigh frequency SAW sensor to various humidity levels, which are increased from 20% to 80% and then decreased from 80% to 20% at room temperature. It can be seen that the frequency shift of the sensor is rapidly increased with the increase of RH and reaches a maximum value of 78 MHz at 80% RH, then the frequency shift is decreased when the RH is reduced to its initial state. The frequency shift versus the humidity change can be drawn using a logarithm format, yielding a linear correlation between relative changes in resonant frequency and RH, as shown in **Figure. 4f**. The linear function was modeled using the equation as follows:

$$\ln \Delta f = a(RH - RH_0) + b \quad (2)$$

where  $RH_0$  is the reference relative humidity,  $\Delta f$  is the frequency shift,  $a$  and  $b$  are constants. The calculated linear regression coefficient is  $\sim 0.9865$ , indicating a good linearity.

The sensitivity (S) of the humidity sensor over a certain humidity range can be determined



using:

$$S = \frac{|\Delta f|}{\Delta RH} \quad (3)$$

where  $\Delta f$  and  $\Delta RH$  are the frequency shifts and humidity changes, respectively. The obtained average value of sensitivity is as high as  $\sim 1.3$  MHz/%RH in a humidity range of 20~80% RH.

The hysteresis of the ultrahigh frequency SAW humidity sensor ( $\lambda=600$  nm) was calculated using the formula,

$$E_{max} = \frac{\Delta m}{Y_{FS}} \times 100\% \quad (4)$$

where  $\Delta m$  is the maximum hysteresis error, and  $Y_{FS}$  is the full-scale output. During the whole testing cycle, the maximum deviation is  $\sim 1.5$  MHz (e.g., at the relative humidity of 70% RH) and the hysteresis is as small as  $\sim 1.92\%$  (**Figure. 4g**)

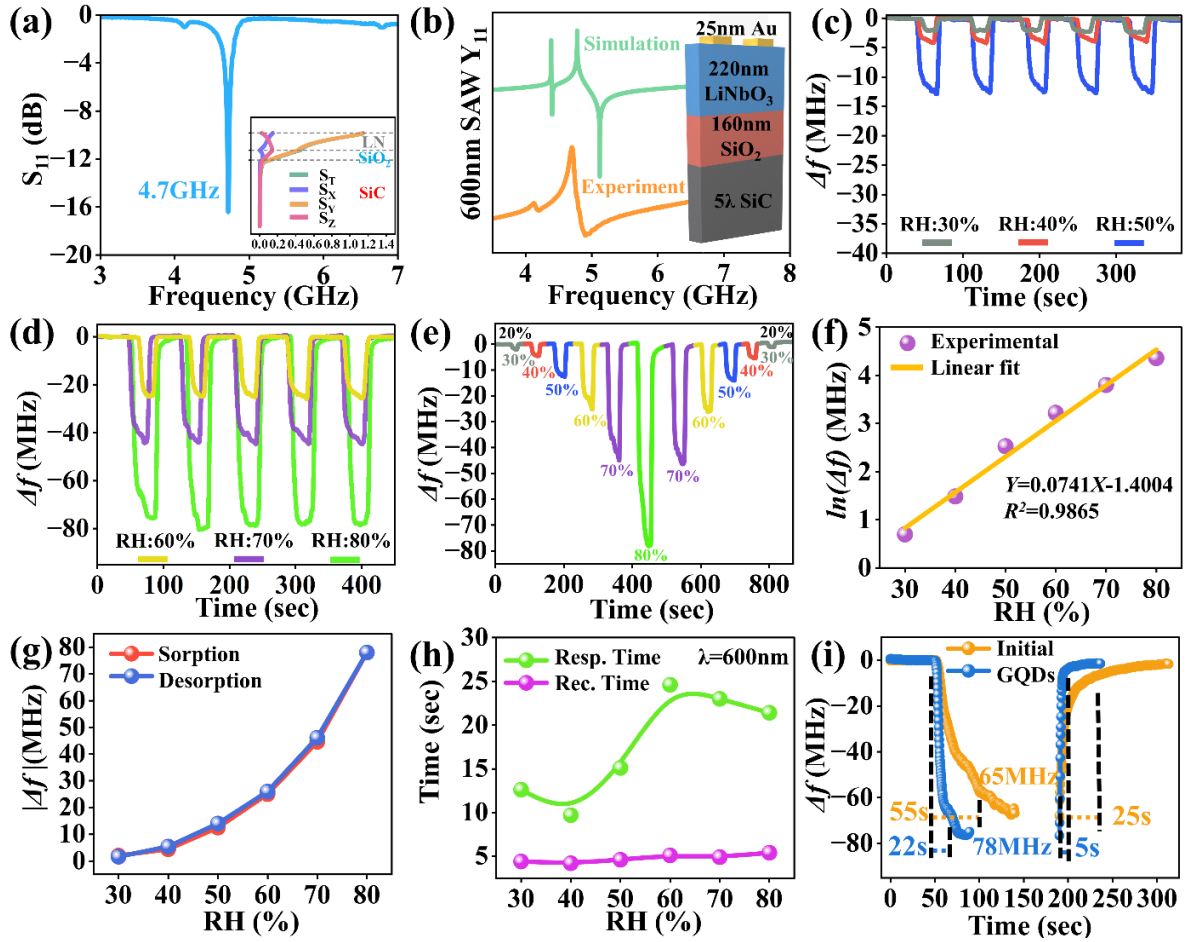


Figure 4: (a) Reflection parameter ( $S_{11}$ ) of ultrahigh frequency SH-SAW device with  $\lambda$  of 600 nm and SH-SAW



---

particle displacement diagram ( $S_T$ : Total displacement,  $S_X$ : X displacement,  $S_Y$ : Y displacement,  $S_Z$ : Z displacement); (b) 3D single-cycle model of the ultrahigh frequency SAW device and simulation/experiment results of  $Y_{11}$  performance; The frequency shift of an ultrahigh frequency SAW humidity sensor ( $\lambda = 600$  nm) through five cycles at six different humidities (c) RH=30%, 40% and 50%; (d) RH=60%, 70% and 80%; (e) Frequency shift results obtained from an ultrahigh frequency SH-SAW humidity sensor ( $\lambda = 600$  nm) within ambient humidity of 20%-80%RH; (f) The  $\ln \Delta f$  versus RH for the SAW humidity sensor ( $\lambda = 600$  nm), showing good linearity relationship; (g) Hysteresis of ultrahigh frequency SH-SAW humidity sensor ( $\lambda = 600$  nm); (h) The response and recovery times of the ultrahigh frequency SAW sensor ( $\lambda = 600$  nm) at various RH levels; (i) The humidity sensing performance of PEI-SiO<sub>2</sub> NPs and GQDs-PEI-SiO<sub>2</sub> NPs on the ultrahigh frequency SAW device ( $\lambda = 600$  nm).

**Figure 4h** shows the response and recovery times of the ultrahigh frequency SAW humidity sensor ( $\lambda = 600$  nm) at different RH levels. The recovery time is ~5s and the response time is 22 s at an RH value of 80%.

We further compared the humidity sensing performance of ultrahigh frequency SAW device using PEI-SiO<sub>2</sub> NPs binary nanocomposite and GQDs-PEI-SiO<sub>2</sub> NPs ternary nanocomposite. **Figure 4i** and **Figure S3a&b** show that after adding the GQDs, the frequency shift was increased from 65 MHz to 78 MHz (i.e., an increase of 20%). The response and recovery times are shortened from 55s/25s to 22s/5s, respectively, under the same RH change from 20% to 80%. Clearly adding the GQDs into the nanocomposite dramatically improves the sensitivity and improves the responsiveness of sensors.

To confirm if the higher frequency leads to a better humidity detection for the ultrahigh frequency SAW devices, we further prepared another ultrahigh frequency SAW device with a



---

smaller wavelength ( $\lambda = 400$  nm), and the resonant frequency is increased to  $\sim 5.9$  GHz, as shown in **Figure 5a**. The simulated particle displacement diagram reveals that this vibration mode is SH-mode. For humidity sensing, similar to the SAW device with  $\lambda$  of 600 nm, the SAW humidity sensor with  $\lambda$  of 400 nm exhibits a high repeatability and stability, with insignificant performance changes under cyclic RH level changes within 20%–80%–20%. However, compared with the SAW device with the frequency of 4.7 GHz ( $\lambda = 600$  nm), the SAW device with a frequency of 5.9 GHz ( $\lambda = 400$  nm) shows a much larger frequency shift at the same humidity change (**Figure 5b**), demonstrating that the increased resonant frequency truly leads to a larger frequency shift with the same humidity changes. **Figure 5c** illustrates the frequency responses of the ultrahigh frequency SAW sensor with a frequency of 5.9 GHz with the humidity levels increased from 20% to 80% and then decreased from 80% to 20% at room temperature. The logarithm values of frequency shifts are linearly correlated with the humidity change (**Figure 5d**) with a linearity of 0.9814. The average humidity sensitivity of 5.9 GHz SAW device was calculated to be  $\sim 2.4$  MHz/% RH (20%-80% RH), which is  $\sim 1.8$  times higher than that of 4.7 GHz SAW device. The hysteresis of the 5.9 GHz SAW device is  $\sim 2.32\%$  (**Figure 5e**), and response/recovery times are about 20s/5s, which are quite similar to those of the 4.7 GHz SAW device. In addition, For the SAW sensor with the resonant frequency of 5.9 GHz, their humidity sensing performance using the GQDs-PEI-SiO<sub>2</sub> NPs ternary nanocomposite as the sensing layer is also much better than that using the PEI-SiO<sub>2</sub> NPs binary ones (**Figure 5f and Figure S3c&d**).

All these results demonstrate that using a GQDs-PEI-SiO<sub>2</sub> NPs ternary sensing layer onto a higher frequency SAW device will lead to better humidity sensing performance. The obtained



humidity detection results are summarized in **Table 1**. Results show that compared with the previously reported SAW humidity sensors reported in literature, our ultrahigh frequency SAW humidity sensor shows the highest humidity average sensitivity (which is 1000 times higher than a conventional 202 MHz SAW devices on LiNbO<sub>3</sub>, and 80 times as high as the 1.56 GHz SAW device with a sensitive layer of CeO<sub>2</sub> nanoparticles/PVP nanofibers) with excellent responsiveness.

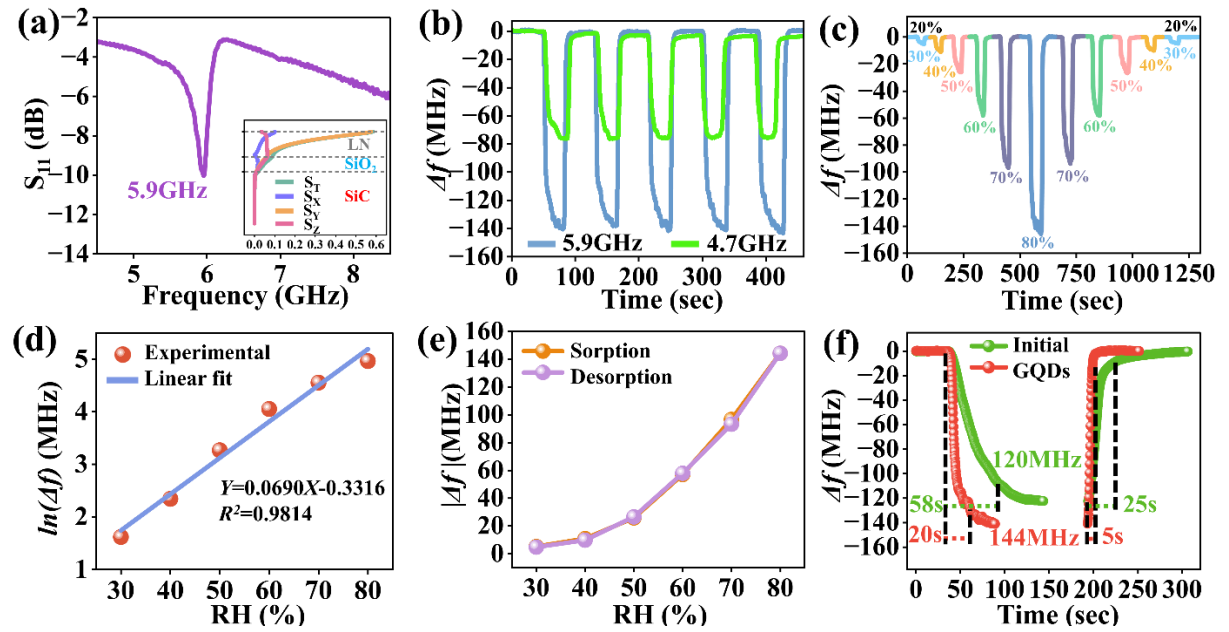


Figure 5: (a) Reflection parameter ( $S_{11}$ ) of ultrahigh frequency SH-SAW device with  $\lambda$  of 400 nm and SH-SAW particle displacement diagram ( $S_T$ : Total displacement,  $S_X$ : X displacement,  $S_Y$ : Y displacement,  $S_Z$ : Z displacement); (b) The frequency shift of ultrahigh frequency SAW humidity sensors ( $f = 4.7\text{GHz}$  and  $5.9\text{GHz}$ ) through five cycles at  $\text{RH} = 80\%$ ; (c) Frequency shift results obtained from an ultrahigh frequency SH-SAW humidity sensor ( $\lambda = 400\text{ nm}$ ) within ambient humidity of  $20\% - 80\% \text{RH}$ ; (d) The  $\ln \Delta f$  versus RH for the SAW humidity sensor ( $\lambda = 400\text{ nm}$ ); (e) Hysteresis of ultrahigh frequency SH-SAW humidity sensor ( $\lambda = 400\text{ nm}$ ); (f) The humidity sensing performance of PEI-SiO<sub>2</sub> NPs and GQDs-PEI-SiO<sub>2</sub> NPs on the ultrahigh frequency SAW device ( $\lambda = 400\text{ nm}$ ).



**Table 1. Comparisons of different SAW-based humidity sensors**

<i>Ref.</i>	<i>Year</i>	<i>f [MHz]</i>	<i>Sensing material</i>	<i>Sensitivity [KHz/% RH]</i>	<i>Measuring range</i>	<i>Resp./Rec. time</i>
[18]	2016	1560	Electrospun CeO <sub>2</sub> NPs/PVP NFs	30	11%~95%	~15/~35s
[8]	2018	222	GO	91	3.6%~98%	600s/6s
[12]	2020	202.5	3DAG/PVA/SiO <sub>2</sub>	2.429	0%-90%	24/14.4s
[13]	2020	220	GQDs/ZnO NMs	40.16	30%-70%	27/12s
[29]	2021	430	SiO <sub>2</sub>	1.14	10%-80%	6/21.3s
[30]	2021	434	Al <sub>2</sub> O <sub>3</sub> Layer	9	0%-98%	50/50s
[31]	2022	200	cellulose acetate	9.46	20%-90%	21/14s
<b>This work</b>	2023	<b>4700</b>	GQDs-PEI-SiO <sub>2</sub>	<b>1300</b>	20%~80%	<b>22/5s</b>
<b>This work</b>	2023	<b>5900</b>	GQDs-PEI-SiO <sub>2</sub>	<b>2400</b>	20%~80%	<b>20/5s</b>

We further investigated the relationship between sensitivity and noise (or stability) of the high frequency SAW devices and low frequency SAW devices. The obtained results are shown in **Figure 6**. **Figure 6a** shows that the noise for the 5.9 GHz SAW device is about 0.62~0.68 MHz with a humidity reading of 20% RH, and it is about 0.92 MHz for a humidity level of 80% RH. For the high frequency SAW device of 4.7 GHz, the noise is 0.55~0.62 MHz for 20% RH, and is 0.81 MHz for 80% RH (**Figure 6b**). Whereas for the low frequency SAW device of 197 MHz, the noise is only 0.013~0.014 MHz for 20% RH, and is 0.013 MHz for 80% RH (**Figure 6c**). Results showed that with the increase of resonant frequency for the SAW device, the noise is indeed increased. Compared with the SAW sensor with a frequency 197 MHz, the noise of SAW sensor with a frequency of 4.7 GHz has been increased by ~57 times, and the noise of



the SAW humidity sensor with a frequency of 5.9 GHz has been increased by ~66 times.

However, it also should be addressed that, the frequency shifts are ~150 MHz, ~80 MHz and ~0.5 MHz, for the SAW devices with their resonant frequencies of 5.9 GHz, 4.7 GHz and 197 MHz, respectively. Compared with the SAW sensor with a frequency 197 MHz, the frequency shift has been increased by ~160 times and ~300 times for the SAW sensors with frequencies of 4.7 GHz and 5.9 GHz. Therefore, increasing the resonant frequency of SAW devices does indeed increase noise, but it also lead to the significant increase in sensitivity, and the increased rate of sensitivity is much higher than that of noise. In addition, based on the results we have obtained, the high frequency device can be well used for the humidity detection with a good stability.

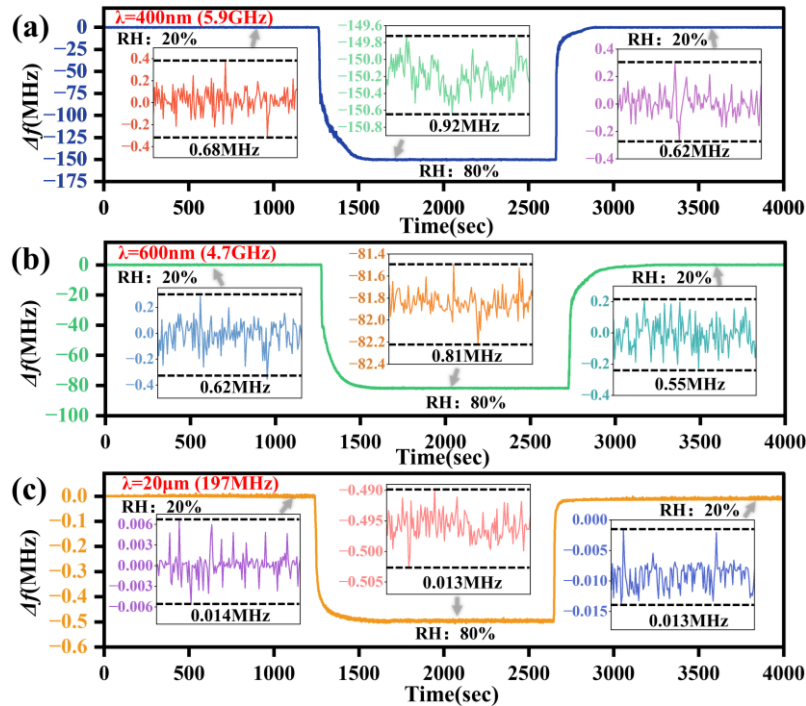


Figure 6: The frequency shift and noise (stability) of SAW humidity sensors with different wavelengths (a):  $\lambda=400$  nm (frequency of 5.9 GHz); (b)  $\lambda=600$  nm (frequency of 4.7 GHz); and (c)  $\lambda=20$   $\mu\text{m}$  (frequency of 197 MHz).

The humidity sensitive materials were GQDs-PEI-SiO<sub>2</sub> NPs for all the SAW devices, and the humidity level was changed from 20% RH to 80% RH, and then back to 20% RH.



---

### 3.3 Bonding and Sensing Mechanisms of Ternary Nanocomposites

The bonding mechanisms of GQDs-PEI-SiO<sub>2</sub> NPs ternary nanocomposite sensing layer on ultrahigh frequency SAW devices were investigated and the results are shown in **Figure 7a**. For the PEI-SiO<sub>2</sub> NPs nanocomposites, the PEI and SiO<sub>2</sub> NPs carry dissimilar electric charges on their surfaces in an aqueous solution, therefore, they were bound together through the electrostatic force [32]. According to the FTIR results (**Figure 3a**), there are a large number of -NH<sub>2</sub> in PEI, while a large numbers of -OH, -COOH and -NH<sub>2</sub> are in GQDs. These chemical groups are prone to forming hydrogen bonds and thus are strongly bound together [28][33]. Hydrogen bonds are also formed between GQDs and PEI-SiO<sub>2</sub> NPs, which attract GQDs strongly adsorbed onto the PEI-SiO<sub>2</sub> NPs to obtain the ternary nanocomposite. Raman spectroscopy analysis (**Figure 3b**) also shows the increase in the I<sub>D</sub>/I<sub>G</sub> ratio of GQDs in ternary materials, which proves the formation of hydrogen bonds.

**Figure 7(b)** illustrates the humidity sensing mechanism of GQDs-PEI-SiO<sub>2</sub> NPs ternary nanocomposite sensing layer. According to widely reported adsorption theory, water molecules in the environment are bound at the hydrophilic points (-OH, -COOH, -NH<sub>2</sub>) in the sensitive materials through the hydrogen bonds [34]. A large number of water molecules are therefore absorbed on the surface of the sensitive material, which increases the mass loading effect, resulting in decreases in the resonant frequency of SAW device. The responses of sensors to humidity are significantly dependent on the types and quantities of exposed hydrophilic groups and the structures of sensitive materials.

The electronegativity of atoms has an important influence on the formation of hydrogen bonds with water molecules. According to the electronegativities of O (3.5) and N (3.0), O-



---

H...O is considered as a much stronger hydrogen bond than the N-H...O [32]. In GQDs-PEI-SiO<sub>2</sub> NPs ternary nanocomposites, there is a large amount of -NH<sub>2</sub> in PEI. This forms N-H...O type hydrogen bonds with water molecules, which are good for humidity sensing. Meanwhile, -OH and -COOH in GQDs can form additional and stronger O-H...O type hydrogen bonds with water molecules. This increases the number and type of hydrophilic groups in the nanocomposite, which can optimize the sensitivity and response/recovery time of the sensor. In addition, the loosely packed and porous sensing layer is conducive to adsorption of water molecule and effective exposure of hydrophilic points. According to the specific surface area results (**Figure 3c**), after modifying and integrating the PEI onto SiO<sub>2</sub> NPs, due to the increases in particle size and agglomeration of SiO<sub>2</sub> NPs, the specific surface area is decreased to a certain extent, but there is still a large specific surface area of 86 m<sup>2</sup>/g. A large number of hydrophilic groups are exposed to the environment, thus providing the PEI-SiO<sub>2</sub> NPs binary nanocomposite with an excellent sensitivity. From the result shown in **Figures 2f** and **3c**, it can be observed that the addition of GQDs makes the surfaces of PEI-SiO<sub>2</sub> NPs much rougher and increases the specific surface areas of the GQDs-PEI-SiO<sub>2</sub> NPs nanocomposite. As a result, introducing additional hydrophilic groups and increasing specific surface areas can expose more hydrophilic sites in GQDs-PEI-SiO<sub>2</sub> NPs, resulting in higher humidity sensitivity of the sensor.

On the other hand, water molecules adsorbed on the surface of nanoparticles can naturally form a convex spherical surface. Due to the surface tension of the liquid, the surface tension on the curved liquid surface cannot be offset, resulting in a combined force directed towards the center of curvature, resulting in additional pressure. According to the Yang-Laplace



equation, the relationship between additional pressure and surface curvature radius is:

$$\Delta p = \frac{2\sigma}{r} \quad (5)$$

where  $\Delta p$  is additional pressure,  $\sigma$  is surface energy,  $r$  is curvature radius, the curvature radius of a convex surface is positive, while the curvature radius of a concave surface is negative.

The additional pressure of water molecules on the convex surface is positive, so their vapor pressure is greater than the environmental pressure, making them more prone to volatilization and easily reaching an equilibrium state [35]. This process corresponds to the response process of the sensor. Therefore, nanoparticles with smaller radius can bring greater vapor pressure and speed up the response of the sensor. According to the characterization results of SEM and TEM (**Figure 2**), the diameter of PEI-SiO<sub>2</sub> NPs is ~30 nm, and the diameter of GQDs is 4-12 nm. The introduction of GQDs reduces the radius of the curved liquid surface formed by water molecules, increases the additional pressure, and significantly improves the response speed. The contrasting results shown in **Figure 4i** and **Figure 5f** proved that this design methodology can significantly optimize the response/recovery time of sensors.

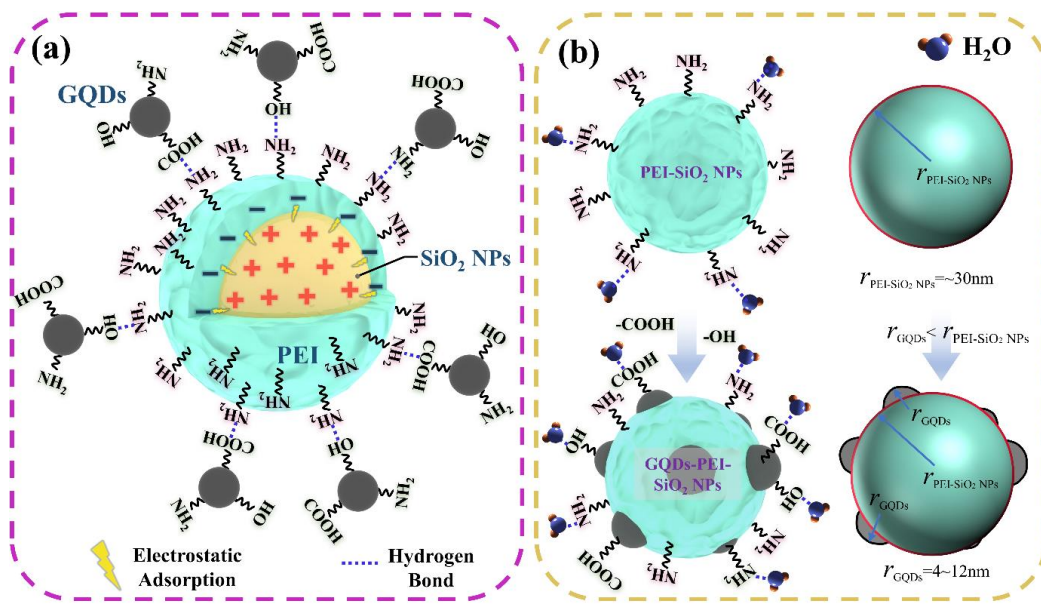


Figure 7: (a) Bonding mechanism of ternary composite material; (b) Humidity sensing principle of ternary



---

composite material.

## **4. Conclusion**

In this paper, ultrahigh frequency SH-SAW devices with their frequencies of 4.7 GHz and 5.9 GHz were fabricated, and a ternary nanocomposite strategy using GQDs-PEI-SiO<sub>2</sub> NPs was proposed as the sensing layer to achieve ultrahigh sensitivity and fast response. The ternary nanocomposite layer was constructed by the modification of PEI, which was then attached onto the surfaces of SiO<sub>2</sub> NPs due to the electrostatic forces, and the GQDs were adsorbed onto the PEI by forming hydrogen bonds with PEI. The achieved humidity sensors show exceptionally high average sensitivity (2.4 MHz/%RH, which is 1000 times higher than that of a convention 202 MHz SAW devices and 80 times as high as the 1.56 GHz SAW devices), fast response (20s/5s), excellent linearity ( $R^2=0.9814$ ), and good repeatability in the range of 20-80% RH. The ultrahigh sensitivity and fast response capability are attributed to the ultrahigh resonant frequency, a large number of hydrophilic groups and the positive pressure of convex spherical curved liquid surface.

## **Author Contributions**

The manuscript was written through contributions of all authors. All authors have given approval to the final version of the manuscript.

## **Notes**

The authors declare no competing financial interest

## **ACKNOWLEDGMENTS**

This work was supported by the NSFC (No.52075162), The Program of New and High-tech Industry of Hunan Province (2021GK4014), The Joint Fund Project of the Ministry of



---

Education, The Excellent Youth Fund of Hunan Province (2021JJ20018), the Key Research & Development Program of Guangdong Province (2020B0101040002), the Engineering Physics and Science Research Council of UK (EPSRC EP/P018998/1) and International Exchange Grant (IEC/NSFC/201078) through Royal Society and the NSFC.

## References

- [1] T.A. Blank, L.P. Eksperiandova, K.N. Belikov, Recent trends of ceramic humidity sensors development: A review, *Sensors and Actuators B: Chemical* 228 (2016) 416-442.
- [2] S. Li, Y. Zhang, X. Liang, H. Wang, H. Lu, M. Zhu, H. Wang, M. Zhang, X. Qiu, Y. Song, Y. Zhang, Humidity-sensitive chemoelectric flexible sensors based on metal-air redox reaction for health management, *Nature Communications* 13(1) (2022) 5416.
- [3] X. Guan, Z. Hou, K. Wu, H. Zhao, S. Liu, T. Fei, T. Zhang, Flexible humidity sensor based on modified cellulose paper, *Sensors and Actuators B: Chemical* 339 (2021) 129879.
- [4] H. Farahani, R. Wagiran, M.N. Hamidon, Humidity Sensors Principle, Mechanism, and Fabrication Technologies: A Comprehensive Review, *Sensors* 14(5) (2014) 7881-7939.
- [5] D. Mandal, S. Banerjee, Surface Acoustic Wave (SAW) Sensors: Physics, Materials, and Applications, *Sensors* 22(3) (2022) 820.
- [6] Y. Tang, Z. Li, J. Ma, L. Wang, J. Yang, B. Du, Q. Yu, X. Zu, Highly sensitive surface acoustic wave (SAW) humidity sensors based on sol-gel SiO<sub>2</sub> films: Investigations on the sensing property and mechanism, *Sensors and Actuators B: Chemical* 215 (2015) 283-291.
- [7] X. Le, Y. Liu, L. Peng, J. Pang, Z. Xu, C. Gao, J. Xie, Surface acoustic wave humidity sensors based on uniform and thickness controllable graphene oxide thin films formed by surface tension, *Microsystems & Nanoengineering* 5(1) (2019) 36.



- 
- [8] I.E. Kuznetsova, V.I. Anisimkin, V.V. Kolesov, V.V. Kashin, V.A. Osipenko, S.P. Gubin, S.V. Tkachev, E. Verona, S. Sun, A.S. Kuznetsova, Sezawa wave acoustic humidity sensor based on graphene oxide sensitive film with enhanced sensitivity, *Sensors and Actuators B: Chemical* 272 (2018) 236-242.
- [9] A. Kawalec, M. Pasternak, A New High-Frequency Surface Acoustic Wave Sensor for Humidity Measurement, *IEEE Transactions on Instrumentation and Measurement* 57(9) (2008) 2019-2023.
- [10] B. Arman Kuzubasoglu, Recent Studies on the Humidity Sensor: A Mini Review, *ACS Applied Electronic Materials* 4(10) (2022) 4797-4807.
- [11] C. Wang, Y. Ding, M. Li, H. Li, S. Xu, C. Li, L. Qian, B. Yang, Surface acoustic wave sensor based on Au/TiO<sub>2</sub>/PEDOT with dual response to carbon dioxide and humidity, *Analytica Chimica Acta* 1190 (2022) 339264.
- [12] Y. Su, C. Li, M. Li, H. Li, S. Xu, L. Qian, B. Yang, Surface acoustic wave humidity sensor based on three-dimensional architecture graphene/PVA/SiO<sub>2</sub> and its application for respiration monitoring, *Sensors and Actuators B: Chemical* 308 (2020) 127693.
- [13] J. Wu, C. Yin, J. Zhou, H. Li, Y. Liu, Y. Shen, S. Garner, Y. Fu, H. Duan, Ultrathin Glass-Based Flexible, Transparent, and Ultrasensitive Surface Acoustic Wave Humidity Sensor with ZnO Nanowires and Graphene Quantum Dots, *ACS Applied Materials & Interfaces* 12(35) (2020) 39817-39825.
- [14] L. Lu, J. Liu, Q. Li, Z. Yi, J. Liu, X. Wang, X. Chen, B. Yang, High Performance SnO<sub>2</sub>/MoS<sub>2</sub>-Based Surface Acoustic Wave Humidity Sensor with Good Linearity, *IEEE Sensors Journal* 19(23) (2019) 11027-11033.



- 
- [15] Y. Pei, X. Zhang, Z. Hui, J. Zhou, X. Huang, G. Sun, W. Huang,  $\text{Ti}_3\text{C}_2\text{TX}$  MXene for Sensing Applications: Recent Progress, Design Principles, and Future Perspectives, *ACS Nano* 15(3) (2021) 3996-4017.
- [16] M. Sajid, Z.J. Khattak, K. Rahman, G. Hassan, K.H. Choi, Progress and future of relative humidity sensors: a review from materials perspective, *Bulletin of Materials Science* 45(4) (2022) 238.
- [17] C. Lv, C. Hu, J. Luo, S. Liu, Y. Qiao, Z. Zhang, J. Song, Y. Shi, J. Cai, A. Watanabe, Recent Advances in Graphene-Based Humidity Sensors, *Nanomaterials* 9(3) (2019) 422.
- [18] Y. Liu, H. Huang, L. Wang, D. Cai, B. Liu, D. Wang, Q. Li, T. Wang, Electrospun  $\text{CeO}_2$  nanoparticles/PVP nanofibers based high-frequency surface acoustic wave humidity sensor, *Sensors and Actuators B: Chemical* 223 (2016) 730-737.
- [19] Z.S. Schroer, Y. Wu, Y. Xing, X. Wu, X. Liu, X. Wang, O.G. Pino, C. Zhou, C. Combs, Q. Pu, M. Wu, J.X. Zhao, J. Chen, Nitrogen–Sulfur-Doped Graphene Quantum Dots with Metal Ion-Resistance for Bioimaging, *ACS Applied Nano Materials* 2(11) (2019) 6858-6865.
- [20] G. Rajender, J. Kumar, P.K. Giri, Interfacial charge transfer in oxygen deficient  $\text{TiO}_2$ -graphene quantum dot hybrid and its influence on the enhanced visible light photocatalysis, *Applied Catalysis B: Environmental* 224 (2018) 960-972.
- [21] E. Wongrat, T. Nuengnit, R. Panyathip, N. Chanlek, N. Hongstith, S. Choopun, Highly selective room temperature ammonia sensors based on  $\text{ZnO}$  nanostructures decorated with graphene quantum dots (GQDs), *Sensors and Actuators B: Chemical* 326 (2021) 128983.
- [22] B. Ramezanzadeh, Z. Haeri, M. Ramezanzadeh, A facile route of making silica nanoparticles-covered graphene oxide nanohybrids ( $\text{SiO}_2$ -GO); fabrication of  $\text{SiO}_2$ -GO/epoxy



---

composite coating with superior barrier and corrosion protection performance, *Chemical Engineering Journal* 303 (2016) 511-528.

[23] J. Fan, D. Li, X. Wang, Effect of modified graphene quantum dots on photocatalytic degradation property, *Diamond and Related Materials* 69 (2016) 81-85.

[24] V. Vatanpour, M. Jouyandeh, H. Akhi, S.S. Mousavi Khadem, M.R. Ganjali, H. Moradi, S. Mirsadeghi, A. Badiei, A. Esmaeili, N. Rabiee, S. Habibzadeh, I. Koyuncu, S. Nouranian, K. Formela, M.R. Saeb, Hyperbranched polyethylenimine functionalized silica/polysulfone nanocomposite membranes for water purification, *Chemosphere* 290 (2022) 133363.

[25] E. Wiercigroch, E. Szafraniec, K. Czamara, M.Z. Pacia, K. Majzner, K. Kochan, A. Kaczor, M. Baranska, K. Malek, Raman and infrared spectroscopy of carbohydrates: A review, *Spectrochimica Acta Part A: Molecular and Biomolecular Spectroscopy* 185 (2017) 317-335.

[26] E. Dervishi, Z. Ji, H. Htoon, M. Sykora, S.K. Doorn, Raman spectroscopy of bottom-up synthesized graphene quantum dots: size and structure dependence, *Nanoscale* 11(35) (2019) 16571-16581.

[27] J.M. Yoo, J.H. Kang, B.H. Hong, Graphene-based nanomaterials for versatile imaging studies, *Chemical Society Reviews* 44(14) (2015) 4835-4852.

[28] H. Guo, T. Jiao, Q. Zhang, W. Guo, Q. Peng, X. Yan, Preparation of Graphene Oxide-Based Hydrogels as Efficient Dye Adsorbents for Wastewater Treatment, *Nanoscale Research Letters* 10(1) (2015) 272.

[29] X. Yan, C. Li, L. Zhao, S. Tian, Z. Zhang, M. Li, H. Li, L. Qian, X. Gong, Y. Huang, T. Hou, H. Bai, B. Yang, Surface acoustic wave relative humidity sensor based on sputtering SiO<sub>2</sub> film, *Surface and Interface Analysis* 53(10) (2021) 867-875.



- 
- [30] S. Alam, U. Mittal, T. Islam, The Oxide Film-Coated Surface Acoustic Wave Resonators for the Measurement of Relative Humidity, *IEEE Transactions on Instrumentation and Measurement* 70 (2021) 1-9.
- [31] W. Wu, X. Xiang, X. Zu, Porous Cellulose Acetate Film-Coated Surface Acoustic Wave Sensor for Highly Sensitive Humidity Sensing, *IEEE Sensors Journal* 22(21) (2022) 20216-20222.
- [32] B. Zhang, X. Yang, X. Liu, J. Li, C. Wang, S. Wang, Polyethyleneimine-interlayered silica-core quantum dot-shell nanocomposites for sensitive detection of *Salmonella typhimurium* via a lateral flow immunoassay, *RSC Advances* 10(5) (2020) 2483-2489.
- [33] L.J. Karas, C.-H. Wu, R. Das, J.I.-C. Wu, Hydrogen bond design principles, *WIREs Computational Molecular Science* 10(6) (2020) e1477.
- [34] L. Lu, C. Jiang, G. Hu, J. Liu, B. Yang, Flexible Noncontact Sensing for Human–Machine Interaction, *Advanced Materials* 33(16) (2021) 2100218.
- [35] N. Li, X.D. Chen, X.P. Chen, X. Ding, X. Zhao, Fast-Response MoS<sub>2</sub>-Based Humidity Sensor Braced by SiO<sub>2</sub> Microsphere Layers, *IEEE Electron Device Letters* 39(1) (2018) 115-118.